FULL PAPER

On the relation between MR spectroscopy features and the distance to MRI-visible solid tumor in GBM patients

Nuno Pedrosa de Barros[1] 🅾 | Raphael Meier[1] | Martin Pletscher[1] | Samuel Stettler[1] |
Urspeter Knecht[1] | Evelyn Herrmann[2] | Philippe Schucht[3] | Mauricio Reyes[4] |
Jan Gralla[1] | Roland Wiest[1] | Johannes Slotboom[1]

[1] University Institute for Diagnostic and Interventional Neuroradiology, University of Bern, Bern, Switzerland

[2] Department of Radiation Oncology, University of Bern, Bern, Switzerland

[3] Department of Neurosurgery, University of Bern, Bern, Switzerland

[4] Institute for Surgical Technology and Biomechanics, University of Bern, Bern, Switzerland

Correspondence
Nuno Pedrosa de Barros, Neuroradiology,
Inselspital, Freiburgstr. 4, CH-3010,
Bern, Switzerland.
Email: nunopbarros@gmail.com
Twitter: @nunopbarros

Purpose: To improve the detection of peritumoral changes in GBM patients by exploring the relation between MRSI information and the distance to the solid tumor volume (STV) defined using structural MRI (sMRI).

Methods: Twenty-three MRSI studies (PRESS, TE 135 ms) acquired from different patients with untreated GBM were used in this study. For each MRSI examination, the STV was identified by segmenting the corresponding sMRI images using BraTumIA, an automatic segmentation method. The relation between different metabolite ratios and the distance to STV was analyzed. A regression forest was trained to predict the distance from each voxel to STV based on 14 metabolite ratios. Then, the trained model was used to determine the expected distance to tumor (EDT) for each voxel of the MRSI test data. EDT maps were compared against sMRI segmentation.

Results: The features showing abnormal values at the longest distances to the tumor were: %NAA, Glx/NAA, Cho/NAA, and Cho/Cr. These four features were also the most important for the prediction of the distances to STV. Each EDT value was associated with a specific metabolic pattern, ranging from normal brain tissue to actively proliferating tumor and necrosis. Low EDT values were highly associated with malignant features such as elevated Cho/NAA and Cho/Cr.

Conclusion: The proposed method enables the automatic detection of metabolic patterns associated with different distances to the STV border and may assist tumor delineation of infiltrative brain tumors such as GBM.

KEYWORDS
expected distance to tumor, GBM, MRSI, nosologic imaging, tumor delineation

1 | INTRODUCTION

Glioblastoma multiforme (GBM) is the most aggressive type of primary brain tumor and is characterized by an extensive infiltration of tumor cells into the tissues surrounding the

tumor.[1] Structural MRI (sMRI) is the imaging technique of reference for the management of GBM patients[2,3] but fails to show the full extent of the infiltrative tumor part,[4] complicating the treatment of this disease.

In order to improve the delineation of these tumors, several research groups[5-8] have used Magnetic Resonance Spectroscopy (MRS), a noninvasive technique that provides metabolic in vivo information of the tissues examined and complements sMRI in the characterization of brain tumors.[9] Results have shown that MRS is able to detect regions with tumor cells outside the tumor limits defined in T_2-weighted images.[8] Improvement in the delineation of glioblastoma has the potential to improve patient treatment and increase the overall survival of these patients, as indicated by a phase II clinical trial[10] where a significant increase in GBM patient's overall survival was observed after incorporating MRS in the planning of radiosurgery. Similarly, during brain surgery, the increased delineation accuracy that can be achieved by using 5-aminolevulinic acid (5-ALA) tumor fluorescence,[11] translates into a more effective tumor resection with increased survival to the patients.[12]

Despite these promising results on the detection of tumor infiltration using MRSI, in the above-mentioned work, as in current clinical practice, only a very limited amount of the information provided by MRS is used. More precisely, the improvement in tumor detection is usually achieved simply by thresholding the metabolite ratio Cho/NAA. Therefore, it is important to evaluate alternative approaches that, using more information, may further improve tumor delineation and detection of tumor infiltration.

Several researchers have developed methods that, instead of analyzing each metabolite or metabolite ratio individually, aim at identifying metabolic patterns associated with different tissues.[13-26] These methods can be divided into two main groups: classification methods[13,18,20,23] and (blind) source separation methods.[14-17,19,21,22,24-26] In the first group the analysis of each spectrum corresponds to the classification of each spectrum into one of a set of predefined classes. Therefore, the tumor boundary is simply the region delimited by the voxels classified as tumoral tissue. In contrast, the second group presents a set of methods that model each spectrum as a linear combination of different reference spectra of predefined tissue-types (e.g., necrosis, tumor, and normal brain tissue). By doing so, tumor delineation can be performed based on the estimations of the tumor-tissue contribution in each spectrum. This type of methods is more suitable for delineating GBM since they are prepared to deal with diffuse tumor boundaries and with partial-volume effects that originate from the low spatial resolution of MRSI data. In both cases, the results can be made easily interpretable by converting the output into nosologic images, that is, images where each color represents a given tissue type.[27]

The two types of methods presented above enable a better use of the MRSI data for tumor delineation, however,

their availability in clinical practice is still very limited. One of the main challenges for the incorporation of such methods into clinical routine is that their results depend on the set of classes or reference spectra used, which not only may vary considerably depending on the dataset and methodology used, but also usually require a nontrivial decision regarding the number of classes or reference spectra that should be considered.

In this work, a novel approach to explore MRSI information for brain tumor delineation is presented. The method was developed considering the solid tumor volume (STV) identified in sMRI as the core of the tumor. Moreover, it was assumed that the probability of finding tumor cells decreases as the distance to the STV increases. Under these assumptions, we explored the relation between metabolic patterns and the distance to the STV defined in sMRI. In this way, it may be possible to detect tumor infiltration by simply identifying metabolic signatures that are associated with close distances to the STV.

The work here presented starts with an analysis of the relation between individual metabolite ratios and the distance to STV. For comparison, we looked also at the values of these metabolite ratios for the different MRI-segmentation classes (white-matter [WM], gray-matter [GM], cerebral-spinal-fluid [CSF], enhancing-tumor [E-Tumor], non-enhancing tumor [NE-Tumor] or necrosis). The analysis of the relation between each feature and the distance to STV was supported by an *MRS-Feature Spatial Distribution* (MRS-FSD) model that is introduced in this article.

After the analysis of the different features separately, a regression forest[28,29] was trained to predict the distance to STV based on the value of 14 metabolite ratios in each spectroscopic voxel. The relation between metabolic patterns and the distances predicted by the regression forest, or expected distances to tumor (EDT), was analyzed. Finally, the contours defined by the EDT maps produced by the trained model were compared with sMRI segmentation.

2 | METHODS

2.1 | Data

A total of 23 pre-operative MRSI examinations (PRESS, CHESS water suppression, TE = 135 ms, TR = 1500 ms) were collected from different GBM patients using two 1.5T Siemens scanners (models "Aera" and "Avanto," Siemens, Erlangen, Germany). The MRSI data had an original resolution of 12 × 12, with a voxel size of 13.33 × 13.33 × 15 mm^3, and was interpolated before DICOM storage to a resolution of 32 × 32 and a voxel size of 5 × 5×15 mm^3. All spectra from outside the PRESS-box, as well as the border voxels of the excited PRESS volumes, were discarded as these voxels are not properly excited. Moreover, the border

voxels of the PRESS volume are usually highly affected by the chemical shift displacement artifact and cannot be corrected using methods such as the selection profile correction discussed in the next section. After removing the outer voxels, the dataset contained a total of 4452 spectra. Besides spectroscopy, the protocol included acquisition of T_1-weighted (MP RAGE, TE = 2.67 ms; TR = 1580 ms, TI = 900 ms; 1 × 1×1 mm), T_{1c}-weighted post-contrast (MP RAGE, TE = 4.57 ms; TR = 2070 ms, TI = 1100 ms; 1 × 1×1 mm), T_2-weighted (SPACE, TE = 380 ms, TR = 3000 ms), and FLAIR MRI (TE = 88 ms, TR = 8000 ms, TI = 2500 ms).

Apart from the data collected from GBM patients, seven MRSI recordings were acquired from three healthy volunteers using the same acquisition parameters. This healthy control dataset contained total of 1372 spectra after exclusion of the outer-voxel row of the excited volume.

The measurements were performed in conformance to local and national ethical regulations, meaning that all patients gave their written informed consent that their data could be used for scientific purposes.

2.2 | MRS data processing pipeline

The MRSI data was processed using jMRUI's SpectrIm plugin (www.jmrui.eu) and included the following processing steps:

1. Residual water peak removal using HLSVD[30];
2. Automatic Quality Control[31-33];
3. Frequency-Shift Correction;
4. Auto-phasing;
5. Quantification using QUEST[34];
6. Selection profile correction.[35]

Quality Control was performed using a random forest model that was trained to reproduce the judgment of an expert. The criteria for rejection of the training data was the presence of visible signal artifacts and low SNR. The trained model outputs a probability of acceptance by an expert. Therefore, after assessing all spectra with the automatic classifier, all spectra with a probability of acceptance by an expert below 0.5 were removed from the dataset. After quality filtering, the dataset contained 3733 spectra, meaning that around 16% of the spectra (719 spectra) were classified as having unacceptable quality. For more details on automatic quality filtering the reader is referred to.[31-33,35]

Quantification was performed using QUEST and a metabolite model that included the following metabolites: Cho, Cr, NAA, Glu, Gln, Lac, Lip1.3, Lip0.9.

Chemical-Shift Displacement artifact and RF selection pulse profile effects of the PRESS sequence were corrected using metabolite maps recorded of phantoms using the same acquisition parameters as the in vivo measurements. This correction is essential for the analysis of MRSI, reducing the spatial variations of the relative metabolite content that originate from the nonideal selection pulses. In-depth information on the selection profile correction is found in Ref. 35.

2.3 | Image segmentation using BraTumIA

The sMRI images acquired for each MRSI examination were segmented into the following compartments: WM, GM, CSF, edema, NE-Tumor, E-Tumor, and necrosis. STV was defined as the union of NE-Tumor, E-Tumor, and necrosis.

The segmentation was performed fully automatically using BraTumIA.[36,37] BraTumIA is a machine learning-based segmentation method that was trained on an independent dataset of 54 pre- and post-operative MRI examinations of glioblastoma that were manually segmented by experienced neuroradiologists. For the automatic segmentation, the following modalities are required as input: T_1, T_{1c}, T_2, and FLAIR. A more detailed description of the algorithm and training data can be found in the study of Meier et al.[37]

2.4 | MRS features

Two types of features were analyzed: (1) *%metabolite*, calculated as the ratio between the area of a given metabolite and the total sum of the areas of all metabolites, and (2) conventional ratios between the areas of two metabolites. The areas were calculated by integration of the complete metabolite signal of the basis set after fitting with QUEST and were corrected for the selection profile. Considering this, the following 14 MRS features were analyzed in this article: %NAA, %Cho, %Cr, %Glx, %Lac, %Lip, Cho/Cr, Cho/NAA, Glx/NAA, Glx/Cr, Lac/Cr, Lip/Cr, Lac/NAA, and Lip/NAA. In these features, Lip stands for the sum of Lip1.3 and Lip0.9, and Glx for the sum of Glu and Gln.

2.5 | Spectra and MRS features for different distances to the STV and different image segmentation classes

For each spectroscopic voxel, the assigned MRI-segmentation class was selected based on majority voting, considering the voxels of the image segmentation mask that are contained within the spectroscopic voxel. Then, the distance from each voxel to the *STV* was calculated as the Euclidean distance to the nearest voxel assigned to one of the classes of the *STV* (*NE-Tumor, E-Tumor, Necrosis*). The distance was calculated in the plane of the MRSI grid and rounded to the closest distance corresponding to an integer number of voxels.

The spectra of all spectroscopic voxels were grouped based on the rounded distance to STV and based on the

segmentation class. All spectra were normalized using L_1-normalization, and, for each group (i.e., range of distances to STV or segmentation class), the median spectra and the 5th, 25th, 75th, and 95th percentile spectra were calculated.

Similarly, to the spectra, the 14 previously described features were also grouped based on the segmentation class and the distance to STV. For each MRSI examination, the different feature maps were spatially interpolated by a factor of four (zero-filling) to enable a finer analysis of the relation between each feature and the distance to STV. After interpolation, the final in-plane resolution was 1.25×1.25 mm. For each distance to STV and for each image segmentation class, the median values as well as the 5th, 25th, 75th, and 95th percentiles were calculated. The same percentiles were calculated for all voxels of the healthy volunteers' dataset and used as a reference.

2.6 | MRS-feature spatial distribution (MRS-FSD) model

In order to compare the spatial properties of the different metabolite ratios, namely their relation with the distance to STV, the following *MRS-Feature Spatial Distribution* (*MRS-FSD*) model was introduced:

$$x_i(d) = K_i + A_i e^{-\frac{d}{\lambda_i}} \quad (1)$$

where d is the distance, and K_i, A_i, and λ_i are the model parameters for the feature i. In this expression, K_i represents the value of the feature i when the distance to the tumor approaches infinity ($K_i = x_i(d=\infty)$). The fit parameter A_i (amplitude) represents the difference between the values found in the STV and the values found in regions far from the STV ($A_i = x_i(d=0) - x_i(d=\infty)$). The distance parameter λ_i, or *spectral feature normalization length*, controls the characteristic rate at which the parameter normalizes as the distance to the tumor increases.

To facilitate the comparison between different features, the values of each feature were rescaled before fitting the model using the following expression:

$$x_i' = \frac{x_i - {}^H X_i^{5th}}{{}^H X_i^{95th} - {}^H X_i^{5th}} \quad (2)$$

where ${}^H X_i^{5th}$ and ${}^H X_i^{95th}$ correspond respectively to the 5th and the 95th percentiles of the same feature in healthy subjects, and x_i and $x\prime_i$ correspond to the value of the feature in GBM patients before and after rescaling. The rescaling enables direct comparison of the different model parameters between different MRS features and allows for an easier interpretation of the results.

Following the above described feature rescaling, we define the abnormality distance of a given feature i, $D_{abn,i}$, as the distance at which each feature crosses the abnormality threshold.

The abnormality threshold was defined as ${}^H X_i^{95th}$ for features that are increased in tumoral tissue relatively to normal brain tissue, and as ${}^H X_i^{5th}$ for features that are decreased in tumoral tissue. Therefore, $D_{abn,i}$ is calculated as:

$$D_{abn,i} = \begin{cases} -\lambda_i \cdot \log\left(\dfrac{1-K_i}{A_i}\right) & , A_i > 0 \\[3mm] -\lambda_i \cdot \log\left(\dfrac{-K_i}{A_i}\right) & , A_i < 0 \end{cases} \quad (3)$$

Spectroscopic features that are, in average, abnormal in large peritumoral volumes are associated with larger $D_{abn,i}$ values.

The *MRS-FSD* was fitted to the median curves of the 14 different features, that is, the curves described by the median feature values in function of the distance to STV. This was motivated by the fact that the number of voxels decreases considerably as the distance to the tumor increases. Moreover, the STV voxels ($d=0$) have often skewed distributions. Finally, the use of the median curves instead of the voxels separately improves the robustness of the results to the presence of outliers.

In order to test the stability of the results, the fitting was performed six times, excluding every time the data from one-sixth of the patients. This was done on par with the sixfold cross-validation scheme used to test the predictions of the distance to the STV described in the following section. The mean and standard deviation of the fitting results were determined.

2.7 | Expected distance to tumor (EDT) maps

To test the ability to identify metabolic patterns associated with different distances to the STV, a regression forest[28] was trained to estimate the distance to solid tumor based on all of the 14 features previously described. For comparison, the distance to the STV was also predicted based on individual features using the corresponding inverted MRS-FSD models. In both cases, the training followed a sixfold cross-validation scheme, where in each iteration the data from one-sixth of the patients were excluded from the training and used to test the trained model.

The regression forests[28] (R, randomForest package[29]) were trained using 500 trees and standard parameters (minimum size of terminal nodes equal to 5, and number features per node equal to one-third of the total number of features,[38] i.e., $14/3 = 4.667 \approx 5$). The trained regressors were used to evaluate which features carry the most information to estimate EDT values. Two different measures of feature importance were analyzed: increase in *Mean Squared Error* (MSE) and *residual sum of squares*. The first one is calculated as the average increase in error as a consequence of permuting the values of a given feature between different Out-Of-Bag (OOB) examples, a group
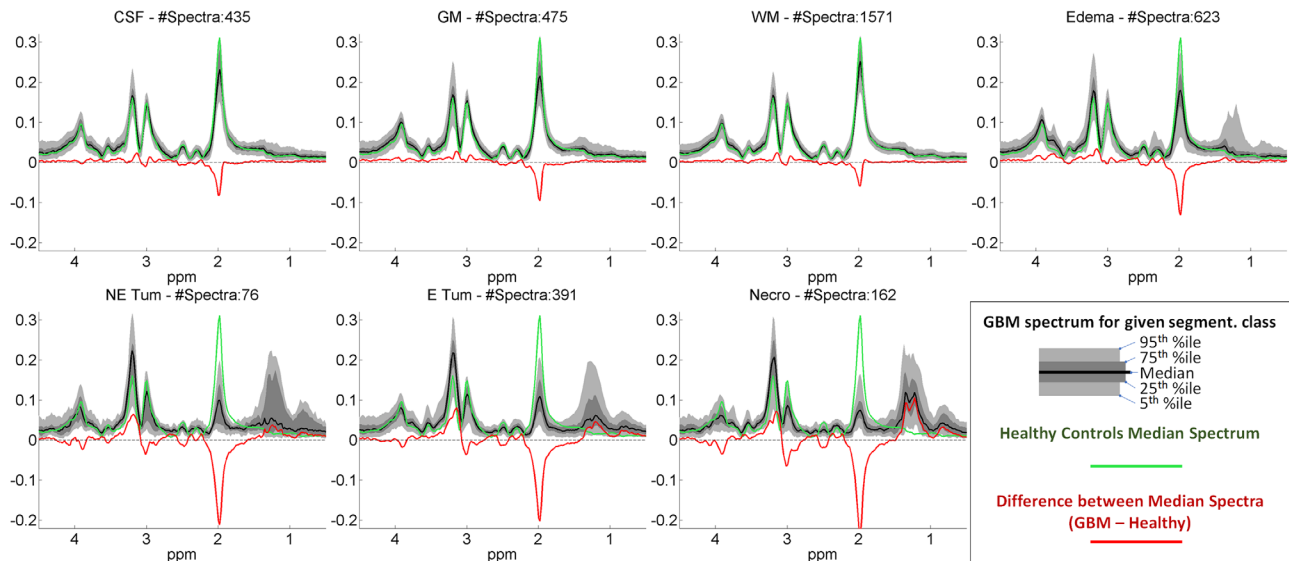
FIGURE 1 Spectra per MRI-Segmentation class. The black line shows the median magnitude spectra for each class and the shades of the gray show the corresponding 5th, 25th, 75th, and 95th percentiles. The green line shows the median magnitude spectra of data collected from healthy controls (includes GM, WM, and CSF), and the red line the difference between the two median magnitude spectra. All spectra were normalized using L_1-normalization. The normal brain tissue pattern seen for the CSF class is a consequence of the partial volume effects and the normalization of the spectra

of examples that are excluded from the training in each tree as a result of *bagging*.[39] The greater the error increase, the greater the importance of the permuted feature for the predictions. Regarding the second measure, the residual sum of squares, this measures the ability of a given feature to separate the examples into different groups with different properties. Features that, during training, have a higher contribution to the separation of the training examples, are considered more important. More details on these feature importance measures that are characteristic of regression forests can be found in the original paper from Breiman.[28]

In order to allow the regression forest models to distinguish the different tumor compartments, virtual distances were assigned to the voxels of these classes before training. A distance of -2 mm was used for necrosis, -1 mm for E-Tumor and 0 for NE-Tumor.

Regarding the estimation of the distance to STV based on the value of a feature i and the corresponding MRS-FSD model, this was determined as:

$$d(x_i) = \begin{cases} -\lambda_i \cdot \log\left(\dfrac{x_i - K_i}{A_i}\right) & , \dfrac{x_i - K_i}{A_i} \geq \varepsilon \\[3mm] -\lambda_i \cdot \log(\varepsilon) & , \dfrac{x_i - K_i}{A_i} < \varepsilon \end{cases} \quad (4)$$

where ε is an arbitrarily small number that, in this work, was defined as 0.001. This prevents problems with close-to-0 and negative arguments of the logarithm function and sets the maximum expected distance that can be predicted using the corresponding model.

3 | RESULTS

3.1 | Spectra per MRI segmentation class

Figure 1 shows the different spectra for each MRI segmentation class. The results show that the spectra vary considerably for each MRI class, especially for the tumor classes. This is caused not only by the differences between the information provided by MRS and sMRI,[40,41] but also by the partial volume effects derived from the low resolution of the acquired MRSI data. Despite the variability, the grouping of the spectra per MRI-segmentation class highlights several distinctive characteristics of the different tissues. As expected, the highest levels of Lip and Lac, and lowest levels of NAA and Cr are normally found in necrosis. Enhancing and NE tumor have very similar spectra, reflecting that contrast leakage caused by blood–brain-barrier disruption does not necessarily translate into differences in metabolic features. Interestingly, in Edema we find the highest levels of Glx (see difference spectrum between 3.7 and 3.8 ppm, and between 2.1 and 2.4 ppm).

Regarding the CSF spectra, pure CSF spectra are expected to contain no metabolites, which conflicts with the results of Figure 1. However, as described in the methods section, each spectrum was assigned to the MRI-segmentation class of the *majority* of the corresponding image voxels. This means that, due to this strategy and the low resolution of the MRSI protocol used, most of the spectroscopic voxels are not "pure" CSF voxels, which explains the existence of visible metabolites in the "CSF" spectra presented here. Moreover, since all spectra are normalized, the height of the peaks in CSF is identical to the one seen in GM or WM.
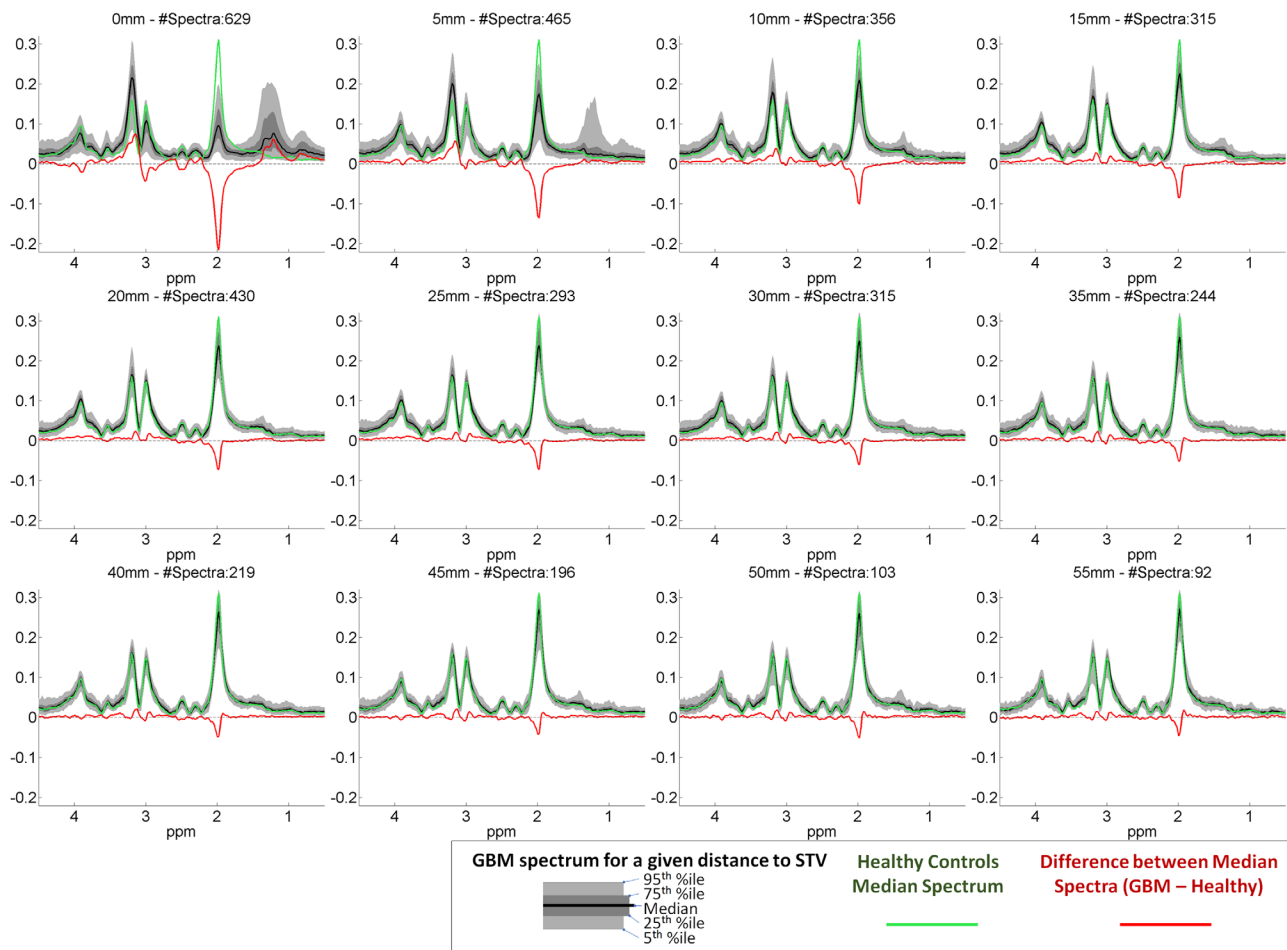
FIGURE 2 Spectra for different distances to the STV. The black line shows the median magnitude spectra for each distance and the shades of the gray show the corresponding 5th, 25th, 75th, and 95th percentiles. The green line shows the median magnitude spectra of data collected from healthy controls (includes GM, WM, and CSF), and the red line the difference between the two median magnitude spectra. All spectra were normalized using L_1-normalization

3.2 | Spectra per distance to the STV

Figure 2 shows the magnitude spectra depending on the distance to the STV. In these plots, a distance of 0 mm corresponds to all spectra of the classes of the STV (E-Tumor, NE-Tumor, Necrosis). By visual inspection, it is difficult to detect changes in distances greater than 30/35 mm. From distances between 5 and 30 mm, the most noticeable effects are the increase in NAA and decrease in Cho as the distance to tumor increases. For distances of 5 mm, some spectra contain elevated levels of lipids, which should come as result of partial volume effects or errors in MRI segmentation. A closer look at the spectra shows that Glx levels are visibly elevated in regions with distances between 5 and 15 mm from the tumor.

3.3 | MRS features as a function of the distance to the STV and image segmentation class

The values of the six *%metabolite* features as a function of the distance (blue) and MRI segmentation class (green) are presented in Figure 3. The reference values of the 5th, 25th, 50th, 75th, and 95th percentiles of each feature in healthy volunteers are shown in red for reference. For sake of simplicity, the plots corresponding to the remaining metabolite ratios are included in the Supporting Information (Supporting Information Figures S1.1 and S1.2).

The data shows that %NAA and %Cr levels are reduced in the brain of GBM patients, even in regions that are located very far from *STV*. As expected, both features get further reduced, as the distance to *STV* decreases. In contrast, the relative quantities of the remaining metabolites increase from normal brain tissue to tumor. The feature %Glx shows a unique characteristic: the maximum value is observed in the peripheral zone of the tumor, in edema and for distances between 5 and 10 mm from the STV.

3.4 | MRS-FSD model

Table 1 shows the results obtained by fitting the MRS-FSD model described (Equation 1) to the rescaled data (see Equation 2). Figure 4 shows a plot of the spectral feature
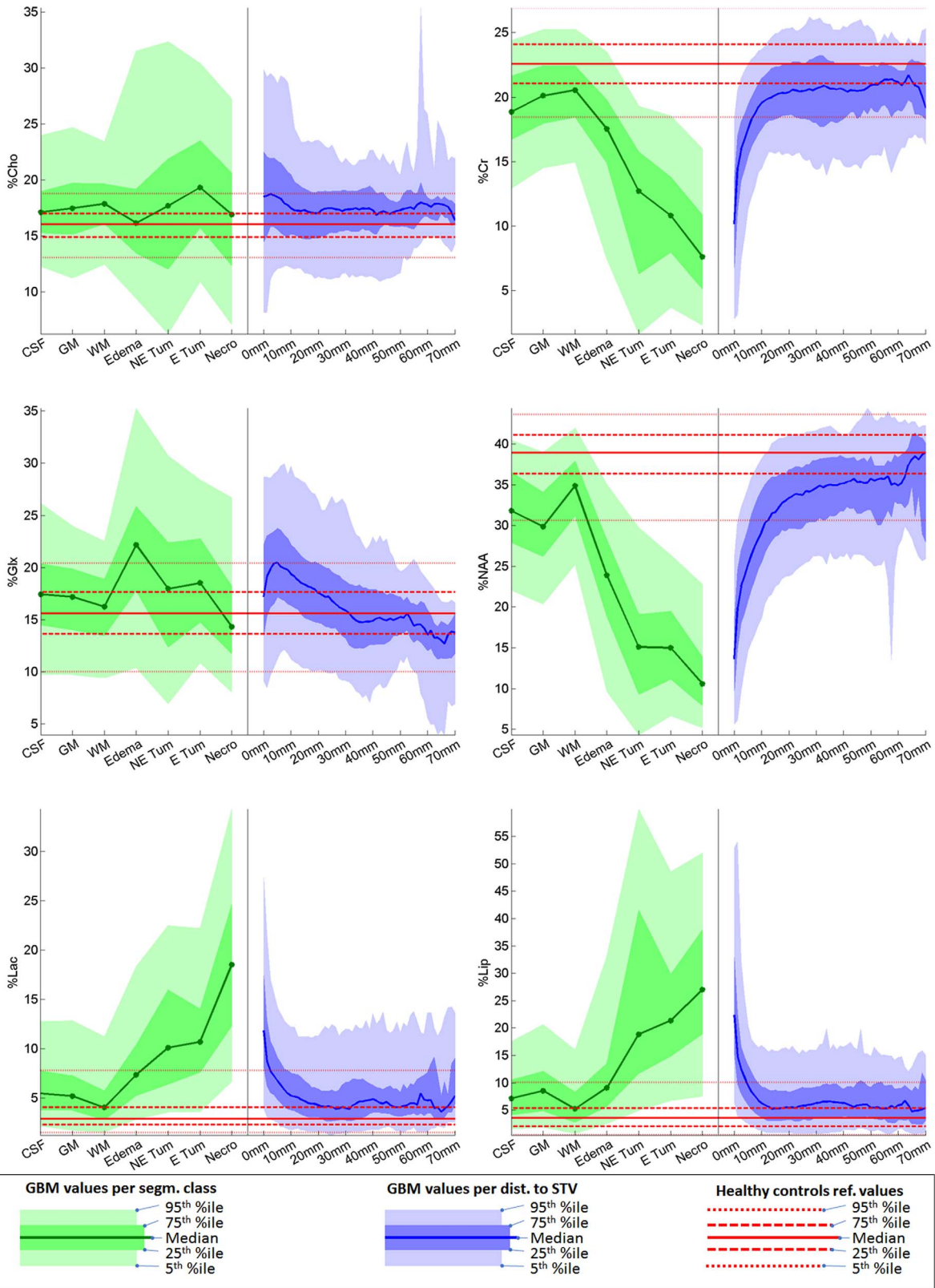
FIGURE 3 Value of several *%metabolite* features as a function of the sMRI segmentation class (green), and the distance to *STV* (blue). For each value of the horizontal axis, the 5th, 25th, 50th, 75th and 95th percentiles are shown as depicted in the legend. For each feature, the horizontal level lines in red mark the 5th, 25th, 50th, 75th, and 95th percentiles in healthy volunteers (includes GM, WM, and CSF)

TABLE 1 Fitting results of the *MRS-FSD* model for different features

Feature	mean R^2	SEM R^2	mean K	SEM K	mean A	SEM A	mean λ	SEM λ	mean D_{abn}	SEM D_{abn}
%Cho	0.470	0.073	0.746	0.008	0.290	0.041	6.963	1.273	0.354	0.730
%Cr	0.943	0.005	0.274	0.014	−1.121	0.018	4.623	0.305	6.479	0.277
%NAA	0.946	0.006	0.406	0.027	−1.484	0.018	9.571	0.802	12.308	0.600
%Glx	0.886	0.008	0.003	0.100	0.996	0.097	60.884	9.453	−0.423	1.140
%Lip	0.925	0.015	0.562	0.011	1.650	0.053	3.043	0.162	4.008	0.119
%Lac	0.848	0.060	0.465	0.017	1.064	0.023	4.393	0.295	3.004	0.179
Cho/NAA	0.967	0.003	0.725	0.020	3.357	0.058	4.230	0.251	10.602	0.558
Cho/Cr	0.975	0.001	0.903	0.012	2.700	0.075	3.162	0.083	10.583	0.265
Glx/NAA	0.959	0.001	0.500	0.017	2.379	0.021	8.706	0.238	13.577	0.235
Glx/Cr	0.948	0.006	0.470	0.014	1.389	0.015	9.409	0.373	9.043	0.263
Lip/Cr	0.959	0.004	0.631	0.009	4.250	0.188	1.915	0.084	4.660	0.150
Lac/Cr	0.930	0.013	0.540	0.011	3.228	0.072	2.183	0.087	4.252	0.161
Lip/NAA	0.961	0.005	0.515	0.012	4.293	0.175	2.064	0.101	4.482	0.158
Lac/NAA	0.930	0.012	0.451	0.017	3.252	0.095	2.547	0.113	4.529	0.205

The model was fitted to the median curve of the feature values in function of the distance to STV. Before curve fitting, the data was rescaled as described in expression 2. For each feature, model fitting was performed six times, excluding every time the data from one-sixth of the patients. The mean and standard error of the mean (SEM) of the fitting results are shown for the coefficient of determination (r^2), model parameters (K, amplitude A, and normalization length λ) and abnormality distance (D_{abn}). Values of λ and D_{abn} are given in mm.

normalization lengths and amplitudes for all ratios except %Glx, for which the normalization length is considerably larger when compared to the remaining metabolites. The introduced model is able to well describe the relation between the feature values and the distance to STV, as shown by the high R^2 values, with the exception of %Cho. For this feature, the differences in value between tumor and healthy brain tissue are close to the level of the noise and, therefore, the model fails to explain a considerable part of the variance of the data. The plots showing the fitting results are included in the Supporting Information (Figures S2.1 to S2.14).

Regarding Glx ratios, Glx/NAA seems to be more sensitive than Glx/Cr to detect the effects of tumor presence, showing a larger normalization length and amplitude. This result can be explained by the fact that, compared to Cr, NAA is reduced in a broader volume that extends farther from the STV, as shown by the larger absolute value of the amplitude and larger normalization length. Given that the increase in Glx has been associated with neuronal loss and demyelination,[42] it is expected that the ratio with NAA increases the sensitivity to detect deterioration and loss of neurons.

The Lip and Lac ratios showed the smallest normalization lengths, reflecting the fact that these features are

significantly altered only in a very confined region, namely in necrotic tissue.

Besides Cho/NAA, whose sensitivity to detect peritumoral changes has been extensively discussed in the literature, two other features stand out as a result of their large abnormality distances: %NAA and Glx/NAA.

3.5 | Expected distance to tumor (EDT)

The feature importance results associated with the regression forest models, as well as the D_{abn} values for each feature, are
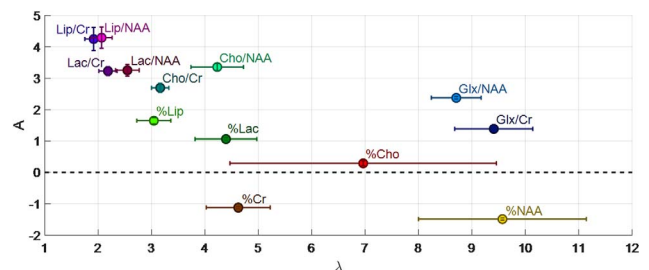

FIGURE 4 Plot of the different amplitudes (*A*) and normalization lengths (λ) for each feature. The plot shows the mean values ± 1.96 times the standard error of the mean of the fitting results shown in Table 1. The results of %Glx are not shown in this plot, given that this feature shows a considerably larger normalization length relative to the other ratios
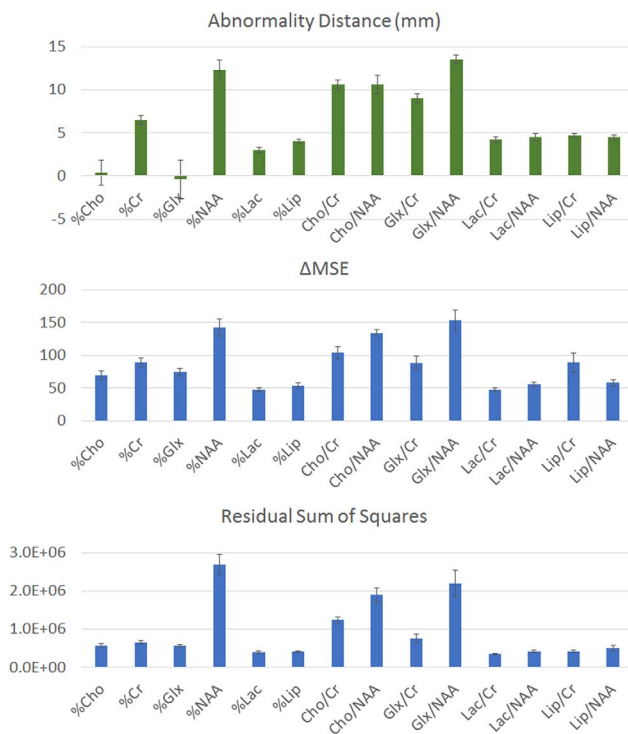
FIGURE 5 Abnormality distances and relative importance for the prediction of the distance to STV of the different MRS features. The abnormality distances (green) were calculated based on the MRS-FSD models for each feature. The two feature importance measures (blue) were determined by the RF-models trained to estimate the distance to the tumor. The bar plots show, for each feature, the mean values ± 1.96 times the standard error of the mean of the sixfold CV results. For a better explanation of the meaning of the feature importance measures please see the Section 2.7

shown in Figure 5. As it can be seen, the abnormality distances are highly correlated with feature importance for the prediction of the distance to STV. The Pearson correlation coefficient between the average values of D_{abn} and ΔMSE was 0.836 ($P = .0002$), and between the average values of D_{abn} and RSS 0.833 ($P = .0002$).

The results show that the four features that contain the most information to estimate the distance to the tumor are %NAA, Glx/NAA, Cho/NAA, and Cho/Cr. From the Lip and Lac related features, Lip/Cr seems to be the most important. Since the different tumor compartments were labeled with different virtual distances (-2 for Necrosis, -1 for E-Tumor, and 0 for NE-Tumor), it is expected that the importance of the Lip/Cr ratio is related to its role in identifying necrotic tissue.

The comparison between the estimated and measured distances to STV for the RF model and for the inverted MRS-FSD models of 5 of the most important features, are presented in Figure 6. Compared to the single-feature models, the predictions made by the RF-model are more accurate and show a smaller variance. However, the predictions of the RF-model show a positive bias for regions close to the STV,

and a negative bias in regions far from the solid tumor. Interestingly, the median curve of the RF-model is approximately monotonic. Due to the superiority of the RF-model, this was the model selected to generate the EDT values used in the following results of this article.

Figure 7 shows the values of different features per EDT and Figure 8 the characteristic spectra associated with different EDT values. These results show the relations between feature values and distance to the STV that were learned by the RF model. The different plots of Figure 8 show that, for each EDT value, there is a specific spectroscopic pattern associated with it. Compared with the results of Figure 2, which show the spectra for different distances to STV, the grouping of the spectra per EDT value shows a better ordering of the spectra in terms of malignancy. More specifically, the ordering per EDT value shows more pronounced malignant features, that is, higher Cho/NAA and Cho/Cr, for shorter (expected) distances and less malignant features, that is, spectra identical to normal brain spectra, for spectra with large (expected) distances to the tumor.

Finally, Figure 9 shows the sMRI segmentation overlaid with the isolines of the corresponding EDT maps. In general, the EDT maps show a good agreement with the sMRI segmentation. However, in several of these maps, regions identified as edema or even normal brain tissue have small EDT values, which, potentially, may indicate regions of tumor infiltration (see, for instance, cases #3, #6, #17, and #18).

4 | DISCUSSION

4.1 | MRS data shows significant metabolic alterations far from solid tumor visible in MRI

The results of Figure 3 show that several of the metabolite ratios are significantly altered in regions outside the STV. Previous studies have shown that MRS is not only able to detect changes being solid tumor visible MRI but also beyond any T_2 abnormalites,[5-8] a characteristic that has been explored to improve tumor delineation. It is expected that the main contribution to the peritumoral changes seen in Figure 3 originate from phenomena of clinical interest, such as tumor infiltration, edema, and inflammatory response. This is supported by the mentioned results from the previous literature, as well as by the structure seen in the peritumoral region that is made visible by the EDT maps of Figure 9. Despite this, the low resolution of the acquired data means that effects caused by signal bleeding,[35,43,44] which causes the voxels near the tumor to have altered spectra regardless of the presence of any tumor-related effect, cannot be ignored. The severity of the signal bleeding depends not only on the native resolution of each MRSI examination but also on other factors such as k-space filtering and on the shape of the source of the signal, in this case, the tumor. The impact that signal bleeding can have on MRSI data can be
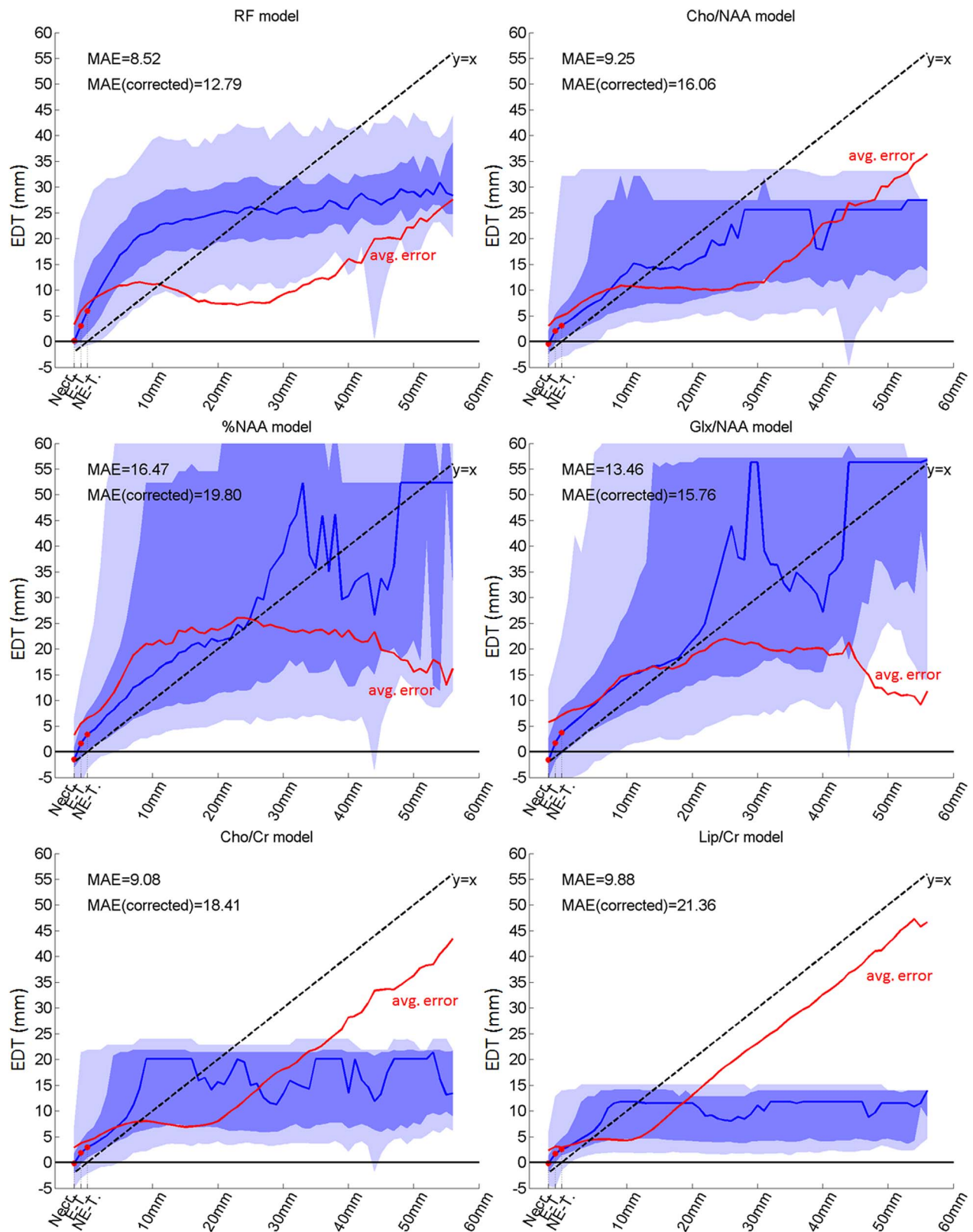
FIGURE 6 Comparison between the predictions of the distance to the STV made using different models. The plots show the predicted distances as a function of the measured distances to the tumor. In each plot, the blue line and the blue shades show the median and the 5th, 25th, 75th, and 95th percentiles of the predicted distances as a function of the measured distances to the tumor, similarly to the shades seen in the plots of Figure 3. The red line shows the mean absolute error in function of the distance to STV. In each plot, the mean absolute error (MAE) for all voxels and corrected MAE are shown. The corrected MAE corrects for the differences in the number of voxels of different distances and corresponds to the average value of MAE for each distance, that is, the average value of the red curve. The virtual distances used to distinguish the different tumor compartments are highlighted in each plot (−2 for Necrosis, −1 for E-Tumor and 0 for NE-Tumor). All results produced using sixfold CV
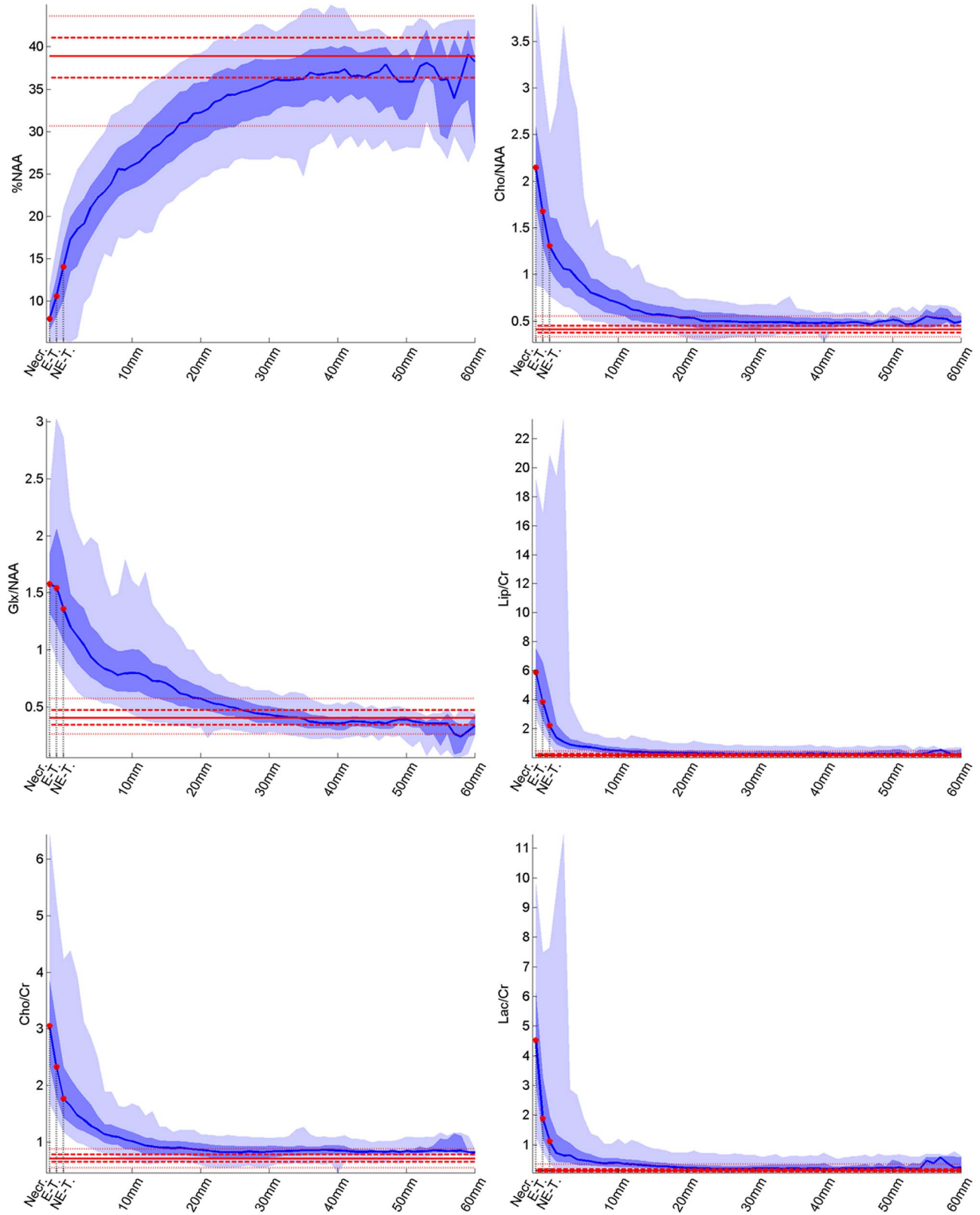
FIGURE 7 Feature values in function of the EDT values predicted using sixfold CV. For each value of the horizontal axis, the 5th, 25th, 50th, 75th, and 95th percentiles are shown (blue shades), as in Figure 3. For each feature, the horizontal level lines in red mark the 5th, 25th, 50th, 75th, and 95th percentiles in healthy volunteers (includes GM, WM, and CSF). The negative and zero EDT values correspond to Necrosis (-2 mm), E-Tumor (-1 mm), and NE-Tumor (0 mm), as it is highlighted in every plot
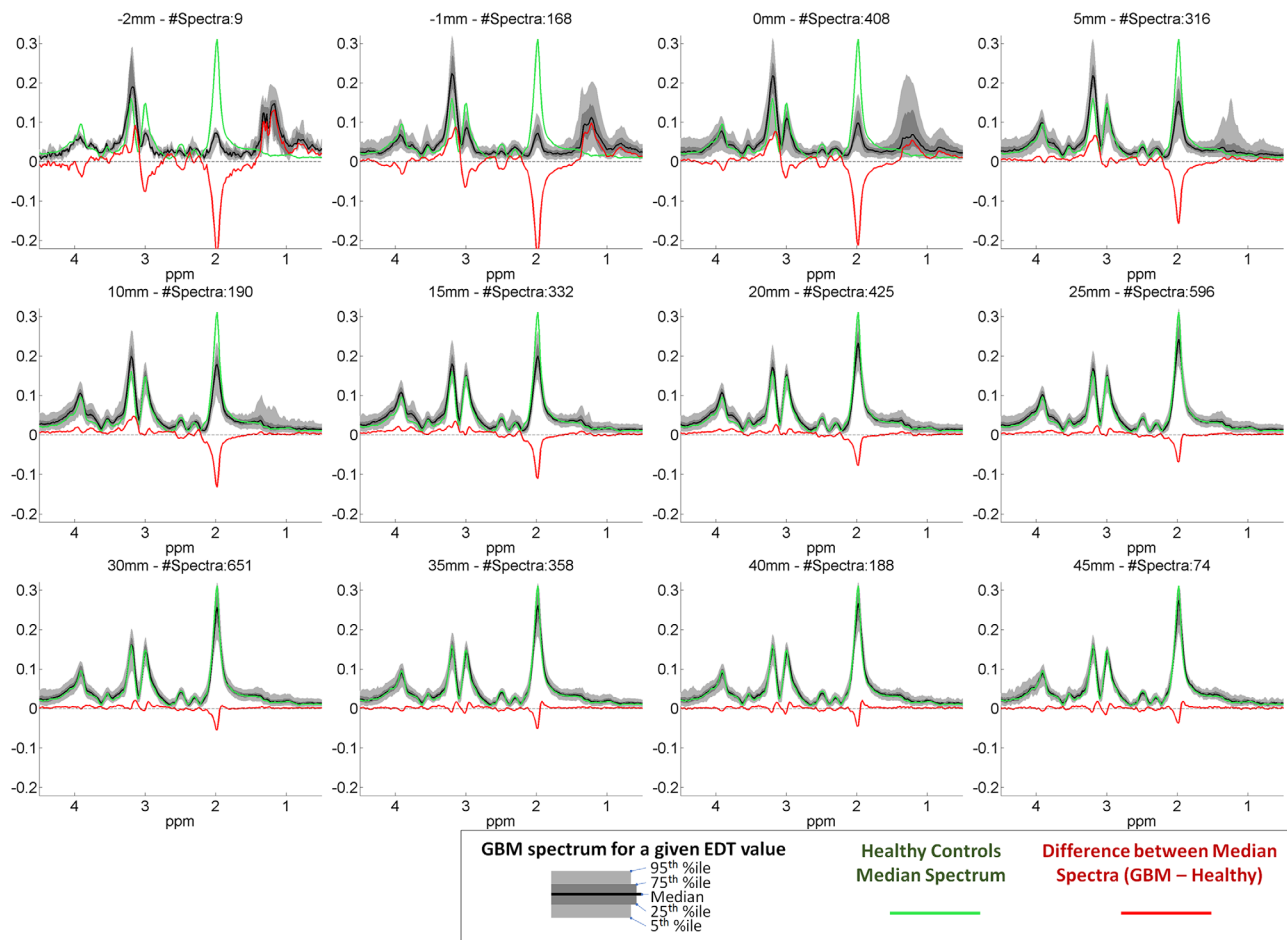
FIGURE 8 Spectra for different EDT values predicted using sixfold CV. EDT values were rounded to the closest distance value shown in these plots. Spectra with EDT values equal or bigger than 47.5 mm were not included. The negative and zero EDT values correspond to Necrosis (-2 mm), E-Tumor (-1 mm), and NE-Tumor (0 mm). The black line shows the median magnitude spectra for each class and the shades of the gray show the corresponding 5th, 25th, 75th, and 95th percentiles. The green line shows the median magnitude spectra of data collected from healthy controls (includes GM, WM, and CSF), and the red line the difference between the two median magnitude spectra. All spectra were normalized using L_1-normalization. No spatial interpolation was performed

assessed by measuring and analyzing the point-spread-function, as described for instance in Ref. 44, or simply performing phantom studies to evaluate the accuracy of tumor delineation as described in Ref. 45. These two aspects should be included in further studies. Besides studies to evaluate the impact of the low resolution in the analysis of the relation between the distance to tumor and MRSI features, it is essential to perform a similar study using higher resolution MRSI data acquired, for instance, with EPSI.[46,47] For an even finer resolution, upscaling of MRSI can be performed based on the structure found in high-resolution MRI images, as shown in Ref. 48. However, in this case, it would be necessary to evaluate the use of the mentioned super-resolution method for brain tumor data.

4.2 | The MRS-FSD model, a tool to analyze the spatial properties of MRS features

The MRS-FSD model introduced in this article describes the main aspects of the relation between each MRS-feature and

the distance to STV. More precisely, the model characterizes each feature in terms of (1) the magnitude and sign of the differences between healthy brain tissue and solid tumor, and (2) the spatial rate of the change. This allows to identify different groups of features: features that are highly altered locally in solid tumor, such as those associated with tumor necrosis like Lip/Cr and Lip/NAA; features that are reduced in solid tumor, such as %Cr and %NAA; and features showing abnormal values in a broad peritumoral region, such as Glx/NAA and %NAA. For the detection of tumor-related changes, the latter group is obviously the most interesting. To help the interpretation of the model parameters, the abnormality distance D_{abn} was introduced. As it was shown, D_{abn} can be used to identify the features that carry the most information for determining the distance to STV. These results, show that the MRS-FSD model is a simple tool that may be used to assist the analysis of the spatial properties of different MRS features in relation to the distance to the solid tumor. Nevertheless, it should be highlighted that the
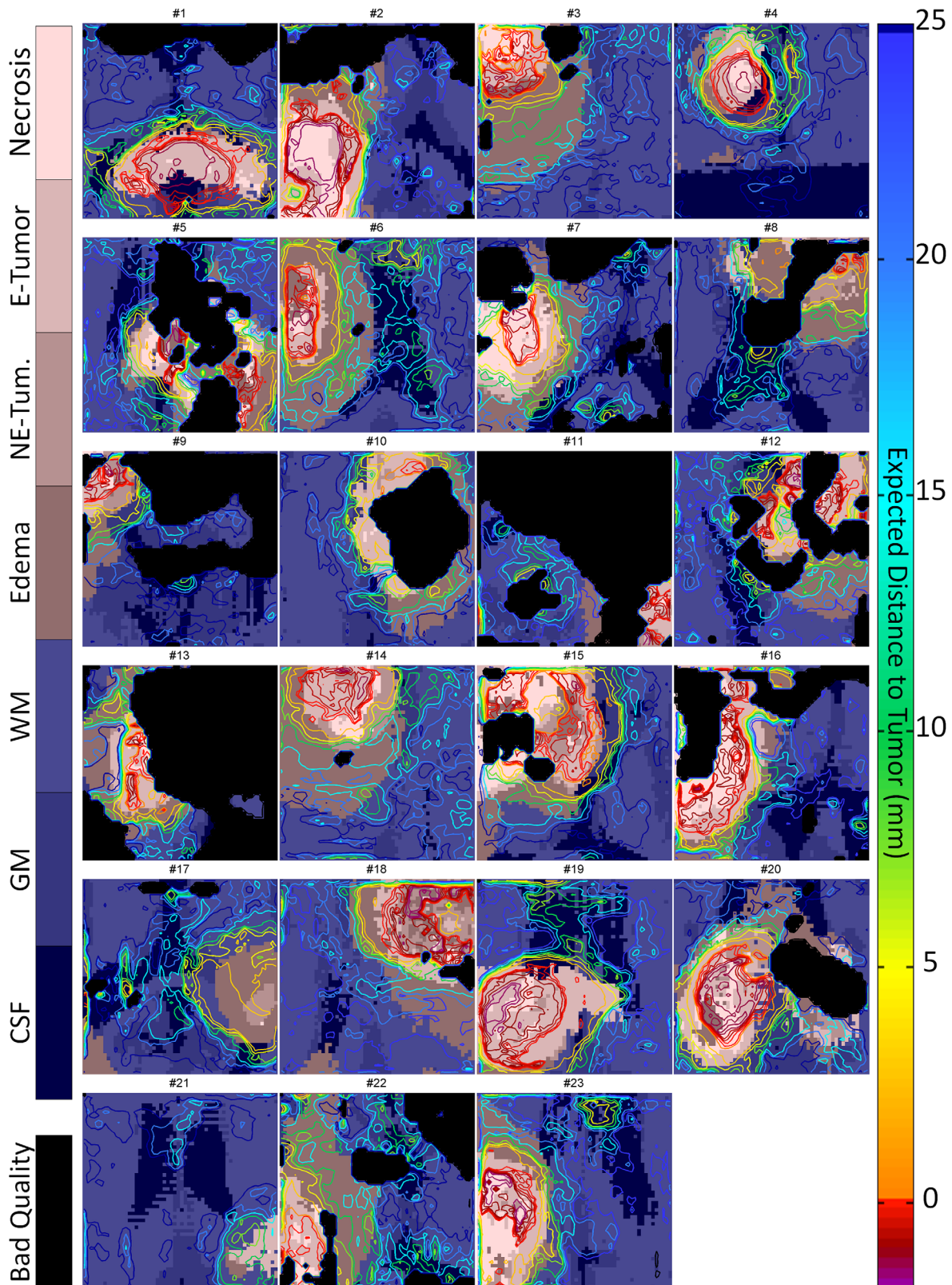
FIGURE 9 Isoline maps of the expected distance to tumor (EDT), determined based on the spectroscopic information from each voxel, overlaid over the corresponding sMRI segmentation. The EDT maps were calculated using the described RF-model and following a sixfold CV scheme, that is, the maps from each row where calculated using models trained based only on the data from the other rows. The color code used for the background image (sMRI segmentation) is shown on the left side. All regions for which the spectra had insufficient quality are shown in black. The color scale of the EDT isolines is shown on the right

simplicity of the model does not allow to completely describe features such as %Glx, for which the maximum values occur neither in STV or healthy brain tissue but in between these two regions.

4.3 | Glx/NAA and %NAA may allow detecting early signs of tumor infiltration

The results in Figure 5 show that %NAA and Glx/NAA are the metabolite ratios with the largest D_{abn}. These features are also the ones that contain the most information for predicting the distance to the STV, followed by Cho/NAA, a metabolite ratio that is known to be associated with tumor infiltration.[5] The ability of Cho/NAA to identify tumor infiltration is justified by the combination of two opposed effects[49-51]: on the one hand, the high membrane turn-over seen in tumor cells leads to high values of (free) Cho and, on the other hand, the neuronal loss/dysfunction as a result of the tumor causes a decrease in NAA. Despite elevated Cho levels being associated with tumor metabolism, the results of Cordova et al.[5] show that Cho/Cr is not a good predictor for tumor infiltration, which may suggest that NAA is the metabolite that mainly explains the correlation between Cho/NAA and tumor cellularity. This is supported by the results presented in this article, showing that %Cho (not to be confounded with the concentration of Cho) is relatively constant regardless of the distance to the tumor or the tumor compartment, in contrast with %NAA, the "%metabolite" feature that shows the biggest differences between normal brain tissue and solid tumor. These results further indicate that %NAA might be a good marker for detecting infiltration. Regarding the ratio Glx/NAA, high values of this ratio can occur as a result of an increase in Glx, which has been associated with inflammation, neuronal loss, demyelination, and tumor proliferation,[42,52,53] combined with a decrease in NAA. This combination of effects suggests that, similarly to %NAA, Glx/NAA might also be an interesting metabolite for the detection of tumor infiltration. Future studies are needed to evaluate the value of these two metabolite ratios for the prediction of tumor infiltration.

4.4 | EDT maps facilitate clinical interpretation of MRSI data

The RF-model trained to predict the distance to the STV based on the different metabolite ratios translates each spectrum into a single EDT value. Moreover, this model was trained to distinguish different tumor compartments, since Necrosis, E-Tumor, and NE-Tumor were labeled with different virtual distances (0 for NE-Tumor, -1 for E-Tumor and -2 for Necrosis). The results shown in Figures 7 and 8 seem to indicate a clear association between

metabolic patterns and EDT values. This characteristic suggests that EDT maps may be regarded as a novel type of nosologic image, allowing an easier clinical interpretation of GBM MRSI data. Moreover, compared to blind source separation methods,[14-17,19,21,22,24-26] no assumptions on the number of basis spectra that need to be considered are required, which may simplify its implementation in clinical practice. Despite this, it would be important to study the correspondence between EDT values and the tissue contributions identified by blind source separation methods.

4.5 | EDT maps may improve detection of infiltration

As described in the previous paragraph, EDT models convert MR spectra into a single "expected distance" that is hypothesized to have a correspondence to a stage in tumor growth. Compared to Cho/NAA thresholding, the RF-based model uses multiple features and is able to learn complex relations between them. Consequently, under the assumption that the probability of tumor infiltration decreases as the distance to STV increases, it is possible that RF-based models may provide a better detection of tumor infiltration than Cho/NAA maps alone. In the case of EDT maps, tumor infiltration is expected to be represented by regions of low EDT values that reflect that these regions share some of the properties seen in regions close to the STV, where infiltration is most likely. An encouraging fact that supports the idea that EDT may help identify infiltration is that, as we see in Figure 6, the RF-model shows that for distances to the STV greater than 20 mm, there is less information for determining EDT values. This suggests that spectra with distances greater than 20 mm are identical to normal brain spectra. These results match the findings described by Pallud et al.,[54] that describe that for diffuse low-grade gliomas MIB-1-positive cells are not normally found in samples collected at distances greater than 20 mm from MRI-defined abnormalities. The relation between EDT maps and tumor infiltration should be validated in future studies. Moreover, it could be interesting to compare the performance for detecting tumor infiltration between the EDT method and blind source separation methods.

4.6 | EDT maps can be easily implemented in clinical practice

The data required to train a new model for generating EDT maps consists of a set of processed MRSI examinations and the corresponding sMRI segmentations. In this work, both the processing of MRSI data and the segmentation of sMRI were performed fully automatically using, respectively, SpectrIm and BraTumIA. Though these two

software applications are currently only available for research, they demonstrate that it is feasible to fully automatically generate the training data based on raw examinations. Once the model is trained, the quantification results of each MRSI examination can be converted into EDT maps almost instantaneously.

The automation of the process of training new EDT models does not only simplify its implementation but also ensures the reproducibility of the results between centers. In case automatic tumor segmentation is not available, semi-automatic methods may also enable reproducible identification of the STV in sMRI.[55]

Finally, another factor facilitating the introduction of the EDT maps in clinical practice is the easy interpretation of the results: an EDT value of 10 mm, for instance, can be easily interpreted as a metabolic pattern that is likely to be found at a distance of 10 mm from the solid tumor border.

Despite these advantages, the results shown in this article can only be regarded as a proof of concept, since clinical validation of the method is currently missing.

5 | CONCLUSION

The results of the presented study confirmed that most ^{1}H-MRS visible metabolites are altered beyond the STV. Moreover, using the MRS-FSD model, it was possible to compare the spatial properties of several of the most commonly used metabolite ratios for the characterization of brain tumors. The analysis suggests that besides Cho/NAA, features such as %NAA and Glx/NAA, which are often significantly altered far from the tumor, may allow detecting early signs of tumor infiltration. Finally, the relation between the distance to the STV and the values of the different metabolite ratios was explored to produce a novel type of map: the EDT maps. This approach converts the information concerning multiple metabolites into a single number, whose value may have a correspondence with the different tissues seen at different stages of tumor growth. EDT maps simplify the interpretation of MRSI data of brain tumor patients and may help to identify early signs of tumor infiltration. Further studies should explore this new concept with higher resolution MRSI data and evaluate its potential application for the diagnosis, follow-up, neurosurgical treatment, and radiotherapy planning of glioma patients.

ORCID

Nuno Pedrosa de Barros http://orcid.org/0000-0003-2403-6705

REFERENCES

[1] Claes A, Idema AJ, Wesseling P. Diffuse glioma growth: A guerilla war. *Acta Neuropathol.* 2007;114:443–458.

[2] Weller M, van den Bent M, Hopkins K, et al. EANO guideline for the diagnosis and treatment of anaplastic gliomas and glioblastoma. *Lancet Oncol.* 2014;15:395–403.

[3] Niyazi M, Brada M, Chalmers AJ, et al. ESTRO-ACROP guideline "target delineation of glioblastomas". *Radiother Oncol.* 2016;118:35–42.

[4] Yamahara T, Numa Y, Oishi T, et al. Morphological and flow cytometric analysis of cell infiltration in glioblastoma: a comparison of autopsy brain and neuroimaging. *Brain Tumor Pathol.* 2010;27:81–87.

[5] Cordova JS, Shu HKG, Liang Z, et al. Whole-brain spectroscopic MRI biomarkers identify infiltrating margins in glioblastoma patients. *Neuro-Oncology.* 2016;18:1180–1189.

[6] Guo J, Yao C, Chen H, et al. The relationship between cho/naa and glioma metabolism: implementation for margin delineation of cerebral gliomas. *Acta Neurochir.* 2012;154:1361–1370.

[7] Stadlbauer A, Moser E, Gruber S, et al. Improved delineation of brain tumors: an automated method for segmentation based on pathologic changes of 1H-MRSI metabolites in gliomas. *NeuroImage.* 2004;23:454–461.

[8] Ganslandt O, Stadlbauer A, Fahlbusch R, et al. Proton magnetic resonance spectroscopic imaging integrated into image-guided surgery: Correlation to standard magnetic resonance imaging and tumor cell density. *Neurosurgery.* 2005;56:291–298.

[9] Hollingworth W, Medina LS, Lenkinski RE, Shibata DK, Bernal B, Zurakowski D. A systematic literature review of magnetic resonance spectroscopy for the characterization of brain tumors. *AJNR Am J Neuroradiol.* 2006;27:1404–1411.

[10] Einstein DB, Wessels B, Bangert B, et al. Phase II trial of radiosurgery to magnetic resonance spectroscopy-defined high-risk tumor volumes in patients with glioblastoma multiforme. *Int J Radiat Oncol Biol Phys.* 2012;84:668–674.

[11] Schucht P, Knittel S, Slotboom J, et al. 5-ALA complete resections go beyond MR contrast enhancement: shift corrected volumetric analysis of the extent of resection in surgery for glioblastoma. *Acta Neurochir.* 2014;156:305–312.

[12] Aldave G, Tejada S, Pay E, et al. Prognostic value of residual fluorescent tissue in glioblastoma patients after gross total resection in 5-aminolevulinic acid-guided surgery. *Neurosurgery.* 2013;72:915–920.

[13] Preul MC, Caramanos Z, Leblanc R, Villemure JG, Arnold DL. Using pattern analysis of in vivo proton MRSI data to improve the diagnosis and surgical management of patients with brain tumors. *NMR Biomed.* 1998;11:192–200.

[14] Sajda P, Du S, Brown TR, et al. Nonnegative matrix factorization for rapid recovery of constituent spectra in magnetic

resonance chemical shift imaging of the brain. *IEEE Trans Med Imaging.* 2004;23:1453–1465.

[15] Du S, Sajda P, Mao X, et al. Multiresolution hierarchical blind recovery of biochemical markers of brain cancer in MRSI. In IEEE International Symposium on Biomedical Imaging: Nano to Macro, 2004. p. 233–236.

[16] Du S, Mao X, Sajda P, Shungu DC. Automated tissue segmentation and blind recovery of1H MRS imaging spectral patterns of normal and diseased human brain. *NMR Biomed.* 2008;21:33–41.

[17] Su Y, Thakur SB, Sasan K, et al. Spectrum separation resolves partial-volume effect of MRSI as demonstrated on brain tumor scans. *NMR Biomed.* 2008;21:1030–1042.

[18] Luts J, Laudadio T, Idema AJ, et al. Nosologic imaging of the brain: segmentation and classification using MRI and MRSI. *NMR Biomed.* 2009;22:374–390.

[19] Ortega-Martorell S, Lisboa PJG, Vellido A, et al. Convex non-negative matrix factorization for brain tumor delimitation from MRSI data. *PLoS One.* 2012;7:e47824.

[20] Lu D, Sun Y, Wan S. Brain tumor classification using non-negative and local non-negative matrix factorization. In 2013 IEEE International Conference on Signal Processing, Communication and Computing (ICSPCC), 2013. p. 1–4.

[21] Li Y, Sima DM, Van Cauter S, et al. Unsupervised nosologic imaging for glioma diagnosis. *IEEE Trans Biomed Eng.* 2013; 60:1760–1763.

[22] Li Y, Sima DM, Cauter SV, et al. Hierarchical non-negative matrix factorization (hNMF): a tissue pattern differentiation method for glioblastoma multiforme diagnosis using MRSI. *NMR Biomed.* 2013;26:307–319.

[23] Yang G, Raschke F, Barrick TR, Howe FA. Manifold Learning in MR spectroscopy using nonlinear dimensionality reduction and unsupervised clustering. *Magn Reson Med.* 2015;74:868–878.

[24] Raschke F, Fellows GA, Wright AJ, Howe FA. 1H 2D MRSI tissue type analysis of gliomas. *Magn Reson Med.* 2015;73: 1381–1389.

[25] Mocioiu V, Pedrosa de Barros N, Ortega Martorell S, Slotboom J, Knecht U, Arús C, et al. A machine learning pipeline for supporting differentiation of glioblastomas from single brain metastases. In ESANN 2016 proceedings: European Symposium on Artificial Neural Networks, Computational Intelligence and Machine Learning: Bruges (Belgium); April 27–29, 2016, I6doc.com; 2016. p. 247–252.

[26] Pedrosa de Barros N, Mocioiu V, Ortega Martorell S, et al. Highlighting differences between GBM and brain metastasis using a blind source separation method applied to MRSI data. In ESMRMB 2015, Edinburgh, UK; 2015.

[27] De Edelenyi FS, Rubin C, Esteve F, et al. A new approach for analyzing proton magnetic resonance spectroscopic images of brain tumors: nosologic images. *Nat Med.* 2000;6: 1287–1289.

[28] Breiman L. Random forests. *Mach Learn.* 2001;45:5–32.

[29] Liaw A, Wiener M. Classification and regression by randomForest. *R News.* 2002;2:18–22.

[30] den Boogaart A, Van Ormondt D, Pijnappel WWF, De Beer R, Ala-Korpela M. Removal of the water resonance from 1H

magnetic resonance spectra. *Math Signal Process.* 1994;3: 175–195.

[31] Pedrosa de Barros N, Mckinley R, Knecht U, Wiest R, Slotboom J. Automatic quality control in clinical 1 H MRSI of brain cancer. *NMR Biomed.* 2016;29:563–575.

[32] Pedrosa de Barros N, Knecht U, McKinley R, Giezendanner J, Wiest R, Slotboom J. Automatic quality assessment of short and long-TE brain tumour MRSI data using novel Spectral Features. In Proceedings of the 24th Annual Meeting of ISMRM, Singapore, 2016.

[33] Pedrosa de Barros N, Mckinley R, Wiest R, Slotboom J. Improving labeling efficiency in automatic quality control of MRSI data. *Magn Reson Med.* 2017;78:2399–2405.

[34] Ratiney H, Coenradie Y, Cavassila S, Van Ormondt D, Graveron-Demilly D. Time-domain quantitation of 1H short echo-time signals: background accommodation. *Magn Reson Mater Phys Biol Med.* 2004;16:284–296.

[35] Pedrosa de Barros N, Slotboom J. Quality management in in vivo proton MRS. *Anal Biochem.* 2017;529:98–116.

[36] Porz N, Bauer S, Pica A, et al. Multi-modal glioblastoma segmentation: man versus machine. *PLoS One.* 2014;9:e96873.

[37] Meier R, Knecht U, Loosli T, et al. Clinical evaluation of a fully-automatic segmentation method for longitudinal brain tumor volumetry. *Sci Rep.* 2016;6:23376.

[38] Hastie T, Tibshirani R, Friedman J. *The Elements of Statistical Learning.* Vol. 1. New York: Springer; 2001.

[39] Breiman L. Bagging predictors: Technical Report No. 421. *Mach Learn.* 1994;140:19.

[40] Lopez CJ, Nagornaya N, Parra NA, et al. Association of radiomics and metabolic tumor volumes in radiation treatment of glioblastoma multiforme. *Int J Radiat Oncol Biol Phys.* 2017;97: 586–595.

[41] Pirzkall A, Li X, Oh J, et al. 3D MRSI for resected high-grade gliomas before RT: Tumor extent according to metabolic activity in relation to MRI. *Int J Radiat Oncol Biol Phys.* 2004;59:126–137.

[42] Ricci R, Bacci A, Tugnoli V, et al. Metabolic findings on 3T 1H-MR spectroscopy in peritumoral brain edema. *Am J Neuroradiol.* 2007;28:1287–1291.

[43] Kreis R. Issues of spectral quality in clinical 1H-magnetic resonance spectroscopy and a gallery of artifacts. *NMR Biomed.* 2004;17:361–381.

[44] Bovée W, Canese R, Decorps M, et al. Absolute metabolite quantification by in vivo NMR spectroscopy: IV. Multicentre trial on MRSI localisation tests. *Magn Reson Imaging.* 1998;16: 1113–1125.

[45] Heikal AA, Wachowicz K, Thomas SD, Fallone BG. A phantom to assess the accuracy of tumor delineation using MRSI. *Radiol Oncol.* 2008;42:232–239.

[46] Posse S, Tedeschi G, Risinger R, Ogg R, Le Bihan D. High speed 1H spectroscopic imaging in human brain by echo planar spatial-spectral encoding. *Magn Reson Med.* 1995;33:34–40.

[47] Sabati M, Sheriff S, Gu M, et al. Multivendor implementation and comparison of volumetric whole-brain echo-planar MR spectroscopic imaging. *Magn Reson Med.* 2015; 74:1209–1220.

[48] Jain S, Sima DM, Sanaei Nezhad F, et al. Patch-based super-resolution of MR spectroscopic images: application to multiple sclerosis. *Front Neurosci.* 2017;11:13.

[49] Oz G, Alger JR, Barker PB, et al. Clinical proton MR spectroscopy in central nervous system disorders. *Radiology.* 2014;270:658–679.

[50] Govindaraju V, Young K, Maudsley AA. Proton NMR chemical shifts and coupling constants for brain metabolites. *NMR Biomed.* 2000;13:129–153.

[51] Mountford CE, Stanwell P, Lin A, Ramadan S, Ross B. Neuro-spectroscopy: the past, present and future. *Chem Rev.* 2010;110: 3060–3086.

[52] Takano T, Lin JH, Arcuino G, Gao Q, Yang J, Nedergaard M. Glutamate release promotes growth of malignant gliomas. *Nat Med.* 2001;7:1010–1015.

[53] DeBerardinis RJ, Cheng T. Q's next: the diverse functions of glutamine in metabolism, cell biology and cancer. *Oncogene.* 2010;29:313–324.

[54] Pallud J, Varlet P, Devaux B, et al. Diffuse low-grade oligoden-drogliomas extend beyond MRI-defined abnormalities. *Neurology.* 2010;74:1724–1731.

[55] Huber T, Alber G, Bette S, et al. Reliability of semi-automated segmentations in glioblastoma. *Clin Neuroradiol.* 2017;27:153–161.

SUPPORTING INFORMATION

Additional Supporting Information may be found online in the supporting information tab for this article.

FIGURE S1.1 and **S1.2** Value of several features as a function of the sMRI segmentation class (green), and the distance to *STV* (blue). For each value of the horizontal axis, the 5th, 25th, 50th, 75th and 95th percentiles are shown as depicted in the legend. For each feature, the horizontal level lines in red mark the 5th, 25th, 50th, 75th and 95th percentiles in healthy volunteers (includes GM, WM and CSF).

FIGURE S2.1 to **S2.14** MRS-FSD fitting results for % Cho (FIGURE S2.1), %Cr (FIGURE S2.2), %Glx (FIGURE S2.3), %NAA (FIGURE S2.4), %Lac (FIGURE S2.5), %Lip (FIGURE S2.6), Cho/Cr (FIGURE S2.7), Cho/NAA (FIGURE S2.8), Glx/Cr (FIGURE S2.9), Glx/NAA (FIGURE S2.10), Lac/Cr (FIGURE S2.11), Lac/NAA (FIGURE S2.12), Lip/Cr (FIGURE S2.13) and Lip/NAA (FIGURE S2.14). In each figure, each plot corresponds to one fold of the 6-fold CV scheme used, where at each time one-sixth of the examinations were excluded from the data used to fit the model. Each plot shows the percentiles per distance to the STV, similarly to what is described in the legend of Figure S1.1 and S1.2. The fitted curves, shown in red, were fitted to the median curves, shown in yellow. The fitting was performed after feature rescaling as described in section 2.6 (after rescaling 0 corresponds to the 5th percentile of the feature in healthy volunteers, and 1 to the 95th percentile). Each plot shows the corresponding coefficient of determination (R2).